Observations of gas flows inside a protoplanetary gap

Simon Casassus[1], Gerrit van der Plas[1], Sebastian Perez M.[1], William R.F.Dent[2,3], Ed Fomalont[4], Janis Hagelberg[5], Antonio Hales[2,4], Andrés Jordán[6], Dimitri Mawet[3], Francois Ménard[7,8], Al Wootten[4], David Wilner[9], A. Meredith Hughes [10], Matthias R. Schreiber[11], Julien H. Girard[3], Barbara Ercolano[12] Hector Canovas[11], Pablo E. Román[13], Vachail Salinas[1]

1. Departamento de Astronomía, Universidad de Chile, Casilla 36-D, Santiago, Chile

2. Joint ALMA Observatory, Alonso de Córdova 3107, Vitacura 763-0355, Santiago - Chile

3. European Southern Observatory (ESO), Casilla 19001, Vitacura, Santiago, Chile

4. National Radio Astronomy Observatory, 520 Edgemont Road, Charlottesville, VA 22903-2475, USA

5. Observatoire de Genève, Université de Genève, 51 ch. des Maillettes, 1290, Versoix, Switzerland

6. Departamento de Astronomía y Astrofísica, Pontificia Universidad Católica de Chile, Santiago, Chile

7. UMI-FCA, CNRS / INSU France (UMI 3386) , and Departamento de Astronomía, Universidad de Chile, Santiago, Chile.

8. CNRS / UJF Grenoble 1, UMR 5274, Institut de Planétologie et dAstrophysique de Grenoble (IPAG), France

9. Harvard-Smithsonian Center for Astrophysics, 60 Garden Street, Cambridge, MA 02138 USA

10. Department of Astronomy, U. C. Berkeley, 601 Campbell Hall, Berkeley, CA 94720

11. Departamento de Física y Astronomía, Universidad Valparaiso, Av. Gran Bretana 111, Valparaiso, Chile.

12. University Observatory, Ludwig-Maximillians University, Munich.

13. Center of Mathematical Modeling, University of Chile, Av. Blanco Encalada 2120 Piso 7, Santiago, Chile.

Gaseous giant planet formation is thought to occur in the first few million years following stellar birth. Models[1] predict that giant planet formation carves a deep gap in the dust component (shallower in the gas[2–4]). Infrared observations of the disk around the young star HD 142527, at ∼140 pc, found an inner disk ∼10 AU in radius[5], surrounded by a particularly large gap[6], with a disrupted[7] outer disk beyond 140 AU, indicative of a perturbing planetary-mass body at ∼90 AU. From radio observations[8,9] the bulk mass is molecular and lies in the outer disk, whose continuum emission has a horseshoe morphology[8]. The vigorous stellar accretion rate[10] would deplete the inner disk[11] in less than a year, so in order to sustain the observed accretion, matter must flow from the outer-disk into the cavity and cross the gap. In dynamical models, the putative protoplanets channel outer-disk material into gap-crossing bridges that feed stellar accretion through the inner disk[12]. Here we report observations with the Atacama Large Millimetre Array (ALMA) that reveal diffuse CO gas inside the gap, with denser HCO$^+$ gas along gap-crossing filaments, and that confirm the horseshoe morphology of the outer disk. The estimated flow rate of the gas is in the range $7\ 10^{-9}$ to $2\ 10^{-7}$ M$_\odot$ yr^{-1}, which is sufficient to maintain accretion onto the star at the present rate.

The HD 142527 system offers an unhindered view of its large central cavity, and is a promising laboratory to observe on-going gaseous giant planet formation. There is good understanding of the orientation of the disk. Multi-wavelength data are consistent with an inclination of ∼20°, so almost face-on[11]. The disk position angle is ~ -20 deg east of north and the eastern side is the far side of the disk, as suggested by a clear view of the outer disk's inner rim in the mid-IR[11,13] and by a clock-wise rotation suggested by a probably trailing spiral arm to the west[6].

We find that the CO(3-2)-emitting gas peaks inside the cavity. Other disks have been observed to exhibit a CO decrement within dust cavities[14,15], and may represent later evolutionary stages or different gap clearing mechanisms. Gas inside dust cavities has previously been directly observed very close to the central star (inside the dust evaporation radius) using near-IR interferometry[16–18]. Other indirect observations of gas inside[19–23] dust gaps at larger distances from the central star have interpreted spectroscopically resolved gas tracers, such as ro-vibrational CO 4.67μm and [O I] 6300Å, under the assumption of azimuthal symmetry and Keplerian rotation. Spectro-astrometry in combination with Keplerian disk models and azimuthal symmetry has also been used to infer the presence of CO gas inside disk gaps[24–26]. Our new data provide a well-resolved observation of gas at

sub-mm wavelengths inside a dust cavity.

The dust gap that we see in radio continuum (Fig. 1 a) indicates a drop by a factor of at least 300 in surface density of mm-sized grains, from the contrast ratio between the peak on the horseshoe-shaped outer disk (the northern peak at 360 mJy beam^{-1}), and the faintest detected signal inside the gap (namely the western filament at 1 mJy beam^{-1}, see below). Yet there is no counterpart in the CO(3-2) map (Fig. 1 b) of the arc that we see in continuum. CO(3-2) is likely optically thick, as reflected by its diffuse morphology, so it traces the temperature profile rather than the underlying density field. Exhaustive modelling of optically thin isotopologue data is required to accurately constraint the depth of the gaseous gap. To study the distribution of dense gas inside the cavity we use the high density gas tracer HCO+.

The second result from our observations is that the HCO^{+}(4-3)-emitting gas, expected in the denser regions ($n_{\mathrm{H2}} \sim 10^{6}$ cm^{-3}) exposed to UV radiation, is indeed found in the exposed rim of the dense outer disk, but also along gap-crossing filaments. The most conspicuous filament extends eastwards from the star, while a fainter filament extends westwards. Both filaments subtend an angle of $\sim 140 \pm 10$ deg with the star at its vertex. The central regions of these filaments correspond to the brightest features in the HCO^{+} line intensity maps (Fig 1 c), although the outer disk is brighter in peak specific intensity (SI, Fig S7). Thus line velocity profiles are broader in the stellar side of the filaments than in the outer disk, where they merge with the outer disk Keplerian rotation pattern. These narrow and systemic velocity HCO^{+} filaments are best seen in intensity maps integrated over the filament velocities (inset to Fig. 1 d). No central peak is seen in the channel maps (SI, Fig. S2), so that a beam-elongation effect can be ruled out. The eastern filament also stands out in peak HCO^{+} specific intensity (SI, Fig. S7 e). For ease of visualization we show deconvolved models of the HCO^{+} intensity images in the inset to Fig. 1 d. A related feature is seen in CO(3-2), whose intensity peaks in the more diffuse regions surrounding the eastern HCO^{+} filament. Interestingly we note from the inset to Fig. 1 a that the continuum also shows features under the HCO^{+} filament, faint and growing away from the walls of the horseshoe-shaped outer-disk. Estimates of physical conditions are given in SI.

The molecular and filamentary flows near the star are non-Keplerian. Blue-shifted emission extends to the east from the central intensity peak (Fig. 1 c). This velocity component is broad near the star, with emission ranging from -3.4 to +11 km s^{-1} (SI, Fig. S2), and is marginally resolved (the central HCO^{+} peak extends over $\sim 0.65 \times 0.38$ arcsec).

3

In the deconvolved images of the inset to Fig. 1 d the peak intensity in the blue and red are separated by ∼0.2 arcsec, i.e. by a diameter of the inner disk, and at a position angle (PA) orthogonal to that expected from close-in high-velocity material in Keplerian rotation. Very blue-shifted emission could reach out to 0.2 arcsec from the star (SI, channel at –2.4 km s^{-1} in Fig. S2, taking into account the beam). A blue-shifted CO(3-2) high-velocity component can also be seen at the root of this feature, near the star (SI, at –2.1 km s^{-1} in Fig. S5).

The non-Keplerian HCO$^+$ is probably not consistent with a central outflow. Stellar outflows are not observed[27] in disks with inner cavities and no molecular envelopes (i.e. transition disks). For an outflow orientation, the low velocities measured by the lines imply that the filaments in HD 142527 would stand still and hover above the star (SI, Sec. 3). Even the blue-shifted emission is slow by comparison to escape velocity. A slow disk wind (e.g. photoevaporative or magnetic driven) can also be excluded on the basis of the high collimation shown by the HCO+ emission. Indeed the CO 4.67 μm seen in the inner disk[26] is purely Keplerian, it does not bear the signature of the disk winds seen in other systems, and its orientation is common to the outer disk. An orthogonal inner disk can be also be discarded on dynamical grounds (SI, Sec. 3).

It is natural to interpret the filaments as planet-induced gap-crossing accretion flows, or 'bridges'. Since the eastern side is the far side, the blue-shifted part of the eastern bridge is directed towards the star, and is a high-velocity termination of the accretion flow onto the inner-disk. These bridges are predicted by hydrodynamical simulations when applied to planet-formation feedback in HD 142527[7]. In these simulations the bridges straddle the protoplanets responsible for the dynamical clearing of the large gap in HD 142527. They are close to Keplerian rotation in azimuth, but do have radial velocity components at $\gtrsim 1/10$ of the azimuthal components. In our data we see that as the bridges land onto the inner disk they also coincide with higher velocity material, at (2-D) radial velocities inferior to their azimuthal velocities in the plane of the sky.

An interesting comparison object is GG Tau. A sub-mm continuum accretion stream[28] is seen to cross the gap in this circum-binary disk, with indications of shocked IR molecular gas in the inner disk[29]. The angular radii of the rings in GG Tau and in HD 142527 are very similar, as are the morphologies of the GG Tau streamer and the eastern filament (although it is fainter relative to the outer disk in HD 142527). However, the GG Tau binary has a mass ratio ∼1 with a separation of 0.25 arcsec, and is aligned along the streamer, while in HD 142527 no stellar companion has been detected (see SI for limits, mass ra-

4

tios are > 10 at 0.088 arcsec). The putative companions responsible for the streams in HD 142527 are much lower mass than in GG Tau.

We performed high-contrast IR imaging to attempt the detection of the possible accreting protoplanets that would be expected if the gap crossing bridges observed in HCO^+ are indeed planet-induced gap-crossing accretion flows. Neglecting extinction, we could virtually rule out any companion more massive than $\sim 4\,M_{jup}$ at separations from 0.3 to 2.5 arcsec (SI, Sec. 4 and Fig. S13, also on the lack of close stellar companions). However, according to the hydrodynamical simulations the channeling protoplanets should be located inside the gap-crossing bridges. Our estimates for N_H along the bridges correspond to a broad range of high extinction values $5 \lesssim A_V \lesssim 50$, for standard dust abundances. Any protoplanets embedded inside the bridges, and certainly those embedded in the dense horseshoe structure, will be obscured, and our mass limits will be correspondingly increased.

A third feature of our observations is the horseshoe shape of the continuum, seen previously by the Sub-Millimetre Array[8] at coarser resolutions, but whose origin is still unclear. The mm continuum traces the total dust mass, so the north-south specific intensity ratio of 28 ± 0.5 reflects the underlying dust mass asymmetry. At its peak the continuum may even be optically thick, as it coincides with a decrease in the HCO+ emission. For a constant gas-to-dust mass ratio, such horseshoe-shaped mass asymmetries arise in models of planet-induced dynamical clearing. In general these horseshoes can be produced by Rossby wave instabilities, which are seen in high-resolution 3D simulations at the edge of sharp density gradients (Varnière private communication). However, horseshoes have also been modelled in the context of large-scale vortices induced by sharp viscosity gradients[30].

Another interpretation for the horseshoe continuum is varying dust-to-gas ratio and azimuthal grain-size segregation. By contrast to the continuum, the outer disk is seen as a whole ring in HCO^+ (Fig. S7), which is a tracer of dense gas, and is probably optically thick along the ring. A rarefaction of mm-sized dust grains to the south could perhaps explain the lack of 345 GHz signal. Only small dust grains would be found in the south. These small grains efficiently scatter the near-IR light seen in Fig. 1 c, filling the opening of the horseshoe. However, azimuthal dust segregation has been predicted for centimetre-sized grains at co-rotation in two-fluid simulations of cavity clearing by giant planet formation[2], while mm-sized grains remain relatively unaffected. We explain in SI why differential stellar heating cannot account for the observed north-south contrast.

The filamentary flows and the residual gas inside the cavity are in qualitative agreement with planet formation feedback on the parent disk, that carves a gap in the dust distribution while still feeding stellar accretion through gap-crossing accretion streams. As detailed in SI, the observed inflow velocity, together with the critical density of the molecular tracer and the section of the filaments, provide a lower bound to the mass inflow rate of $7 \ 10^{-9} \ \mathrm{M}_\odot \ \mathrm{yr}^{-1}$. An upper bound of $2 \ 10^{-7} \ \mathrm{M}_\odot \ \mathrm{yr}^{-1}$ can be estimated from the continuum mass in the filaments and their kinematic timescale. These estimates for the mass inflow rate are close to the observed stellar accretion rate[10] of $7 \times 10^{-8} \ \mathrm{M}_\odot \ \mathrm{yr}^{-1}$, bringing quantitative support to our suggestion that the HCO^+ filaments are inflows.

1. Lubow, S. H. & D'Angelo, G. Gas Flow across Gaps in Protoplanetary Disks. *Astrophys. J.* **641**, 526–533 (2006). `arXiv:astro-ph/0512292`.

2. Fouchet, L., Gonzalez, J.-F. & Maddison, S. T. Planet gaps in the dust layer of 3D protoplanetary disks. I. Hydrodynamical simulations of T Tauri disks. *Astron. Astrophys.* **518**, A16 (2010). `1005.5600`.

3. Ayliffe, B. A., Laibe, G., Price, D. J. & Bate, M. R. On the accumulation of planetesimals near disc gaps created by protoplanets. *Mon. Not. R. Astron. Soc.* **423**, 1450–1462 (2012). `1203.4953`.

4. Zhu, Z., Nelson, R. P., Hartmann, L., Espaillat, C. & Calvet, N. Transitional and Pretransitional Disks: Gap Opening by Multiple Planets? *Astrophys. J.* **729**, 47 (2011). `1012.4395`.

5. van Boekel, R. *et al.* The building blocks of planets within the 'terrestrial' region of protoplanetary disks. *Nature* **432**, 479–482 (2004).

6. Fukagawa, M. *et al.* Near-Infrared Images of Protoplanetary Disk Surrounding HD 142527. *Astrophys. J.* **636**, L153–L156 (2006).

7. Casassus, S. *et al.* The Dynamically Disrupted Gap in HD 142527. *Astrophys. J.* **754**, L31 (2012). `1207.2056`.

8. Ohashi, N. Observational signature of planet formation: The ALMA view. *Astrophys. Space Sci.* **313**, 101–107 (2008).

9. Öberg, K. I. *et al.* Disk Imaging Survey of Chemistry with SMA. II. Southern Sky Protoplanetary Disk Data and Full Sample Statistics. *Astrophys. J.* **734**, 98–+ (2011). `1104.1236`.

10. Garcia Lopez, R., Natta, A., Testi, L. & Habart, E. Accretion rates in Herbig Ae stars. *Astron. Astrophys.* **459**, 837–842 (2006). `arXiv:astro-ph/0609032`.

11. Verhoeff, A. P. *et al.* The complex circumstellar environment of HD 142527. *Astron. Astrophys.* **528**, A91+ (2011). `1101.5719`.

12. Dodson-Robinson, S. E. & Salyk, C. Transitional Disks as Signposts of Young, Multiplanet Systems. *Astrophys. J.* **738**, 131 (2011). `1106.4824`.

13. Fujiwara, H. *et al.* The Asymmetric Thermal Emission of the Protoplanetary Disk Surrounding HD 142527 Seen by Subaru/COMICS. *Astrophys. J.* **644**, L133–L136 (2006). `arXiv:astro-ph/0701808`.

14. Lyo, A.-R., Ohashi, N., Qi, C., Wilner, D. J. & Su, Y.-N. Millimeter Observations of the Transition Disk around HD 135344B (SAO 206462). *Astron. J.* **142**, 151–160 (2011). `1108.5840`.

15. Mathews, G. S., Williams, J. P. & Ménard, F. 880 μm Imaging of a Transitional Disk in Upper Scorpius: Holdover from the Era of Giant Planet Formation? *Astrophys. J.* **753**, 59 (2012). `1205.3545`.

16. Tatulli, E. *et al.* Constraining the wind launching region in Herbig Ae stars: AMBER/VLTI spectroscopy of HD 104237. *Astron. Astrophys.* **464**, 55–58 (2007). `arXiv:astro-ph/0606684`.

17. Kraus, S. *et al.* The origin of hydrogen line emission for five Herbig Ae/Be stars spatially resolved by VLTI/AMBER spectro-interferometry. *Astron. Astrophys.* **489**, 1157–1173 (2008). `0807.1119`.

18. Eisner, J. A. *et al.* Spatially and Spectrally Resolved Hydrogen Gas within 0.1 AU of T Tauri and Herbig Ae/Be Stars. *Astrophys. J.* **718**, 774–794 (2010). `1006.1651`.

19. Carr, J. S., Mathieu, R. D. & Najita, J. R. Evidence for Residual Material in Accretion Disk Gaps: CO Fundamental Emission from the T Tauri Spectroscopic Binary DQ Tauri. *Astrophys. J.* **551**, 454–460 (2001). `arXiv:astro-ph/0101059`.

20. Najita, J., Carr, J. S. & Mathieu, R. D. Gas in the Terrestrial Planet Region of Disks: CO Fundamental Emission from T Tauri Stars. *Astrophys. J.* **589**, 931–952 (2003).

21. Acke, B. & van den Ancker, M. E. Resolving the disk rotation of HD 97048 and HD 100546 in the [O I] 6300 Å line: evidence for a giant planet orbiting HD 100546. *Astron. Astrophys.* **449**, 267–279 (2006). `arXiv:astro-ph/0512562`.

22. van der Plas, G. *et al.* The structure of protoplanetary disks surrounding three young intermediate mass stars. I. Resolving the disk rotation in the [OI] 6300 Å line. *Astron. Astrophys.* **485**, 487–495 (2008). `0802.0707`.

23. Salyk, C., Blake, G. A., Boogert, A. C. A. & Brown, J. M. High-resolution 5 μm Spectroscopy of Transitional Disks. *Astrophys. J.* **699**, 330–347 (2009).

24. Pontoppidan, K. M. *et al.* Spectroastrometric Imaging of Molecular Gas within Protoplanetary Disk Gaps. *Astrophys. J.* **684**, 1323–1329 (2008). `0805.3314`.

25. van der Plas, G. *et al.* Evidence for CO depletion in the inner regions of gas-rich protoplanetary disks. *Astron. Astrophys.* **500**, 1137–1141 (2009). `0810.3417`.

26. Pontoppidan, K. M., Blake, G. A. & Smette, A. The Structure and Dynamics of Molecular Gas in Planet-forming Zones: A CRIRES Spectro-astrometric Survey. *Astrophys. J.* **733**, 84 (2011). `1103.3000`.

27. Sacco, G. G. *et al.* High-resolution Spectroscopy of Ne II Emission from Young Stellar Objects. *Astrophys. J.* **747**, 142 (2012). `1201.0184`.

28. Piétu, V., Gueth, F., Hily-Blant, P., Schuster, K.-F. & Pety, J. High resolution imaging of the GG Tauri system at 267 GHz. *Astron. Astrophys.* **528**, A81 (2011). `1102.4029`.

29. Beck, T. L. *et al.* Circumbinary Gas Accretion onto a Central Binary: Infrared Molecular Hydrogen Emission from GG Tau A. *Astrophys. J.* **754**, 72 (2012). `1205.1526`.

30. Regály, Z., Juhász, A., Sándor, Z. & Dullemond, C. P. Possible planet-forming regions on submillimetre images. *Mon. Not. R. Astron. Soc.* **419**, 1701–1712 (2012). `1109.6177`.

Supplementary Information additional figures, information on instrumental setups and physical condition estimates.

Contributions   General design of ALMA project, data analysis and write-up: SC. Discussion of IR observations of gas in cavities: GvdP. Hydrodynamical modeling: SP. ALMA data reduction: AH, EF. ADI processing: DM, JH, JG. Contributions to ALMA Cycle 0 proposal: AJ, FM, DW, MH. Design of ALMA observations: AW, AH, SC. Authors WD to AW contributed equally. All authors discussed the results and commented on the manuscript.

Competing Interests   The authors declare that they have no competing financial interests.

Correspondence   Correspondence and requests for materials should be addressed to S.C. (email: scasassus@u.uchile.cl).
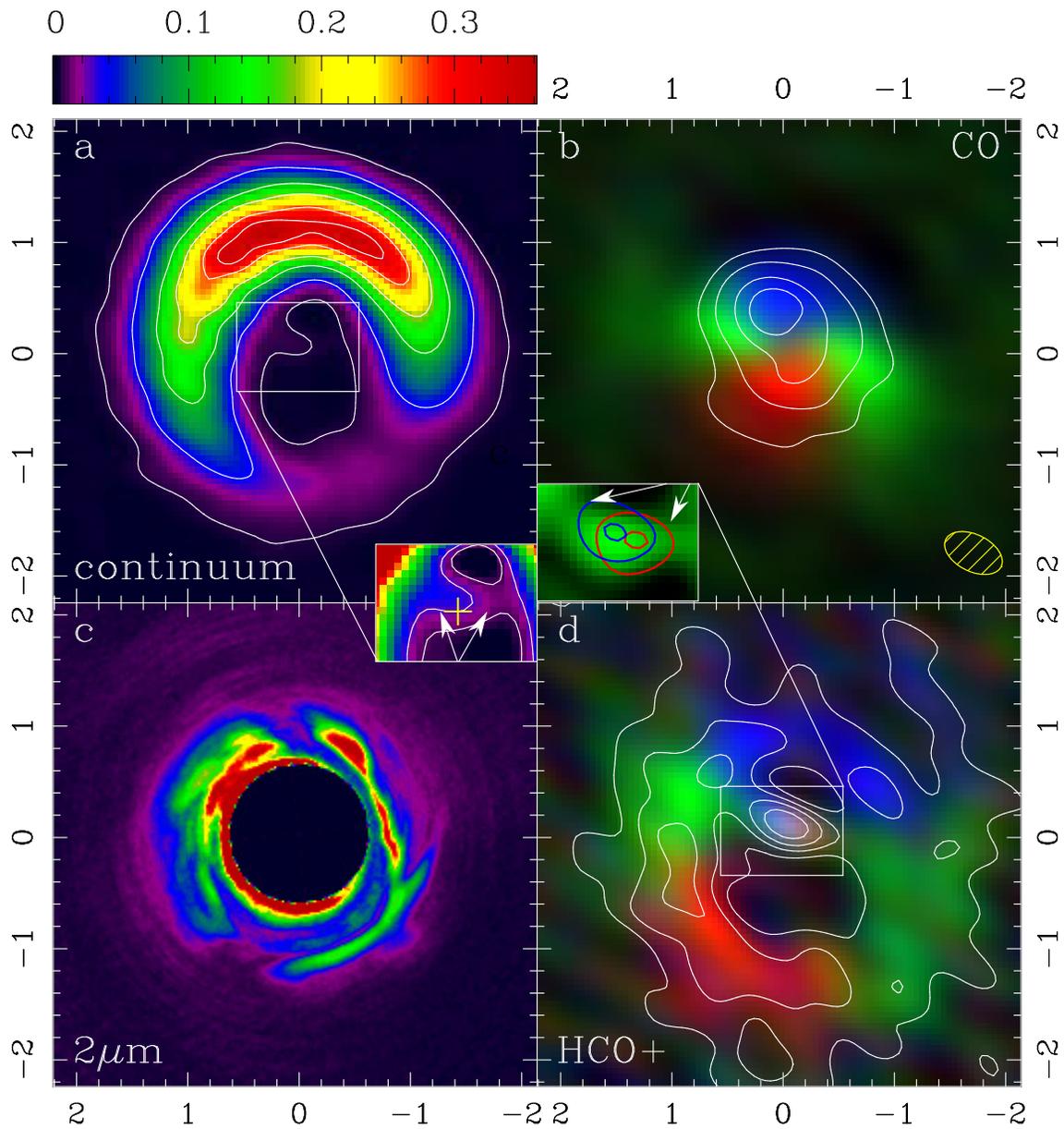
Figure 1 **ALMA observations of HD 142527, with a horseshoe dust continuum surrounding a cavity that still contains gas.** We see diffuse CO gas in Keplerian rotation (coded in doppler-shifted colours), and filamentary emission in HCO⁺, with non-Keplerian flows near the star (comparison models illustrative of Keplerian rotation are shown in SI). The near-IR emission abuts onto the inner rim of the horseshoe-

10

shaped outer disk. The star is at the origin of coordinates and axis labels are in arcsec; North is up, East is to the left. **a:** The image labelled 'continuum' is a CLEANed image of the continuum at 345 GHz, with specific intensity units in Jy beam^{-1}. It is shown in exponential scale. A beam ellipse is shown in the bottom right, and contour levels are taken at 0.01, 0.1, 0.3, 0.5, 3/4, 0.9 times the peak value. The noise level is 1 σ =0.5 mJy beam^{-1}. **b:** The image labelled 'CO' is CO(3-2) line intensity in white contours at fractions of 0.3, 0.5, 0.75 and 0.95 of the peak intensity value $2.325 \ 10^{-20}$ W beam^{-1}. The underlying RGB image also shows CO(3-2) line intensity but integrated in three different velocity bands, whose velocity limits are indicated in the spectra of Fig. S8. **c:** The image labelled '2 μm' is a near-IR image from Gemini that traces reflected stellar light, shown in linear scale. We applied an circular intensity mask to the stellar glare, some of which immediatelly surrounds the mask. See Fig. S1 in SI for an overlay with the continuum. **d:** The image labelled 'HCO$^+$' shows HCO$^+$(4-3) line intensity in white contours at fractions of 0.1, 0.3, 0.5, 0.75 and 0.95 of the peak intensity value $0.40 \ 10^{-20}$ W beam^{-1}, overlaid on an RGB image of HCO$^+$ intensity summed in three different colour bands, with definitions in Fig. S8. **Insets:** Zoom on the central features that cross the dust gap. The cross indicates the star at the origin, with a 0.05 arcsec accuracy, and the arrows point at the filaments. Fig. 1 a inset: same as Fig. 1 a, with a narrow exponential scale highlighting the gap-crossing filaments. Note how these features appear to grow from the eastern and western sides of the horseshoe. Contours are at at 0.0015 and 0.005 Jy beam^{-1}. Fig. 1 d inset: deconvolved models (see SI) of the HCO$^+$ emission at velocities where the gap-crossing filaments are seen, i.e. from 3.2 to 4.3 km s^{-1}, in green. Intensity maps for the blue and red velocity ranges (see Fig. S8 for definitions) are shown in contours, with levels at 0.5 and 0.95 of the peak values. These red and blue contours are an alternative way to present the intensity field shown in Fig. 1 d, but deconvolved for ease of visualization.

Supplementary Information

1 ALMA Observations

Instrumental setup and data reduction

ALMA setup. ALMA Band 7 observations of HD142527 were carried out in the night of June 2 2012. The precipitable water vapor in the atmosphere was stable between 1.4 and 1.8 mm, with clear sky conditions. The ALMA correlator was configured in the Frequency Division Mode (FDM) to provide 468.750 MHz bandwidth in four different spectral windows at 122.07 kHz resolution (0.1 km/s) per channel. Each spectral window was positioned in order to target the CO(3-2) transition at 345.7959 GHz, HCO+ as well as CS(7-6) and HCN(4-3). The measured system temperatures ranged from 207 to 285 K in the different spectral windows. The number of 12 m antennas available at the time of the observation was 19, although two antennas reported very large system temperatures (DA41 and DV12) and were flagged during data reduction. Excluding calibration overheads, a total time on source of 52 minutes was spent yielding an RMS of 15 mJy in 0.1 km s^{-1} channels. The primary flux calibrator was Titan, which provided a mean transferred flux of 14.2 Jy for 3c279, the bandpass calibrator, and 0.55 Jy for J1604-446, the phase calibrator. Amplitude calibration used the CASA Butler-JPL-Horizons 2010 model for Titan, which gives an estimated systematic flux uncertainty of $\sim$10%. All the line data were processed with continuum subtraction in the visibility domain.

Image synthesis. Image synthesis was performed using two different techniques, depending on the application. For a traditional way to present the visibility dataset we use Cotton-Schwab `CLEAN` in the `CASA` package. This technique represents the consensus in image synthesis. We use Briggs weighting with robustness parameter of zero. For deconvolved models we use a non-parametric least-squares modeling technique[1] with a regularizing entropy term (i.e. as in the family of maximum entropy methods, MEM here and elsewhere). MEM model images are restored by convolving with the clean beam and by adding the residuals calculated using the `difmap` package[2]. For the residuals we use weights comparable to our choice in `CASA`, a mixture of natural and uniform weights. A detailed example of this MEM algorithm is shown in the HCO$^+$ channel maps, Fig. S4.

Registration of ALMA images. A ~0.1 arcsec astrometric uncertainty could affect the ALMA data. However, we checked the astrometry by confirming that the centroid of the Keplerian velocity field (seen in the RGB image for CO(3-2) in Fig. 1) lies indeed at the position of HD 142527 in J2000 at the June 2012 epoch (J2000 15:56:41.878 -42:19:23.568). The near-IR scattered light images[7], which are centred on the stellar position, are matched by the inner boundary of the sub-mm thermal continuum, as expected. This match is illustrated in Fig. S1. Overall, we estimate that any astrometric error is less than ~0.05 arcsec.

Self-calibration of continuum maps. A continuum image visibility dataset was constructed from the nominal calibration of the source data, covering all ALMA spectral windows but excluding line channels. The restored continuum image peaked at 0.38 Jy beam^{-1}, with a noise level (including artifacts from negative sidelobes) of $6\ 10^{-3}$ Jy beam^{-1}, giving a dynamic range of 63. The image was clearly limited by phase errors. We therefore applied self-calibration. Using the nominal calibration image as a model of the source, we used the self-calibration algorithm to determine improved antenna-based phases that were consistent with the image. The solution interval chosen was 5 min, long enough to give over 30:1 signal to noise (2 deg accuracy) per antenna solution. The measured residual phases varied smoothly over the experiment, with a typical value of 5 to 10 deg. After applying these small phase corrections, the rms noise on the new image was 20% of the original rms, and the weak southern part of the outer disk became clearly visible. With this improved model, the next self-calibration iteration also included the antenna gain variations which were typically five percent or less. This second round of self-calibration decreased the rms a further 50%. The final image has a peak of 0.38 Jy beam^{-1} and an rms of $5.2\ 10^{-4}$ Jy beam^{-1}, so of the order of the theoretical noise level, which is 10% of the original rms. Since the dynamic range of the nominal calibration was 63, even the stongest line emission in 1 km s^{-1} channels, after subtraction of the continuum emission, was receiver noise limited rather than dynamic range limited. Hence, self-calibration correction to the line channels were not needed.

Presentation of the ALMA data

Channel maps. The HCO^{+} channel maps in Fig. S2 illustrate the off-center high-velocity flows, and the gap-crossing filaments at a velocity close to that of the star (the systemic velocity). These filaments are seen more clearly in the deconvolved channel maps shown in Fig. S4. The CO(3-2) channel maps shown in Fig. S5 also highlight the blue-shifted part of the high-velocity flows seen in HCO^{+}.

2

HCO$^+$ peak and intensity maps. We use the same set of CLEANed HCO$^+$ images from 5-channel averages as in the channel maps to summarize the basic features of the HCO$^+$ emission through moment maps. Fig. S7a exposes in more detail the total intensity map shown in Fig. 1. The peak intensity map in Fig S7c illustrates that the outer disk is a whole ring in HCO$^+$.

Line spectra. The first column in Fig. S8 shows spectra extracted from CLEAN reconstructions, using the same aperture as show on Fig. 1. The right column shows the corresponding MEM spectra. The spectrum labelled 'streamer', in bottom right, corresponds to the inset of Fig. 1 d.

2 Comparison disk models

To illustrate the expected kinematics in Keplerian rotation we have calculated a disk model using the LIME[3] package. This model is inclined at 20 deg, with a PA of -20 deg east of north, and is placed at a distance of 140 pc with a 2.7 M$_\odot$ central star. The distance of 140 pc is supported by a probable association to Sco OB2.

For CO we assumed an abundance of 10^{-4} relative to H$_2$ and the following number density distribution of H$_2$ molecules:

$$n_{\mathrm{H2}}(r, z) = 1.5 \ 10^{14} \ \left(\frac{r}{100 \ \mathrm{AU}}\right)^{-1.5} \ \exp\left[-\frac{1}{2}\left(\frac{z}{0.1 \ r}\right)^2\right] \ \mathrm{m}^{-3},$$

from 140 to 300 AU, and

$$n_{\mathrm{H2}}(r, z) = \zeta \ 1.5 \ 10^{14} \ \exp\left[-\frac{1}{2}\left(\frac{z}{0.1 \ r}\right)^2\right] \ \mathrm{m}^{-3},$$

from 10 to 140 AU, and zero elsewhere. $\zeta = 1/10$ is a fiducial well-depth. The total mass in this disk model is 0.1 M$_\odot$. The temperature profile is $T(r) = 50 \ [r/(50 \ \mathrm{AU}]^{-1/2} \ K$, as inspired from the observed CO(3-2) peak with a radiation temperature of 50 K.

For HCO$^+$ we assumed a relative abundance of 10^{-7}, a mass distribution as for CO but without material inside the gap, and the same temperature profile.

We filtered the LIME predictions to match the uv-coverage of the data, and we

reconstructed the resulting visibility in the same way as the observations. Resuts for CO(3-2) are shown in Fig. S10 and Fig. S5. In the case of HCO$^+$ the line is weaker so we subtracted the continuum. We also added a central elongated source to assess the effects of beam elongation, see Fig. S2. We conclude that beam elongation effects cannot mimic the HCO$^+$ filaments.

3   Physical conditions

Conditions along the filaments   An estimate of physical conditions in the filaments can be obtained by assuming that the CO(3-2) emission is optically thick. If so the peak CO(3-2) specific intensity of 0.9 Jy beam^{-1} in a 0.55×0.33 arcsec^2 beam corresponds to a kinetic temperature of 50 K. The peak HCO$^+$ specific intensity is 0.1 Jy beam^{-1} or $\sim$5.7 K in radiation temperature. This implies HCO$^+$ columns of $N_{\mathrm{HCO+}} \sim 5\ 10^{14}$ cm^{-2}. Densities in excess of $n_{\mathrm{H2}} \sim 10^5$ cm^{-3} are required to excite HCO$^+$(4-3) and if the streamers are as deep as they are wide ($\sim 5\ 10^{14}$ cm corresponding to 0.25 arcsec), we expect H-nucleus columns $N_H > 10^{20}$cm^{-2}. We thus have an upper bound on the HCO$^+$ abundance of $N_{\mathrm{HCO+}}/N_H < 5\ 10^{-6}$. A lower bound is placed by the observed (cosmic-ray induced) ionization fraction in cold cores[4] of $\sim 10^{-8}$. In summary, from HCO$^+$ we have $5\ 10^{22} \gtrsim N_H/\mathrm{cm}^{-2} \gtrsim 10^{20}$. The observed continuum under the filaments ranges from 0.4 mJy beam^{-1} to 5.6 mJy beam^{-1} before beeing confused with the wall, and the corresponding columns are $1.3\ 10^{23} \gtrsim N_H/\mathrm{cm}^{-2} \gtrsim 8.5\ 10^{21}$. Extinction values can be estimated using a standard formula[5], $N_H/\mathrm{cm}^{-2} = 1.87\ 10^{21} A_V$.

Physicality of central outflows   On first impression, star formation experts would interpret the non-Keplerian HCO$^+$ as a stellar outflow. The orientation of the eastern filament is indeed roughly orthogonal to the disk PA, and outflows are expected in the context of stellar accretion. However, planet-induced accretion may not require outflows to dissipate angular momentum (whose bulk has been dissipated earlier by powerful stellar outflows during the general protostellar accretion). Outflows have optical/IR counterparts, but no extended emission is seen in our Brγ imaging from Gemini (SI). In general outflows are not seen in transition disks[27] (class II young stars with disks and an inner cavity). Here we consider the plausibility of a ballistic outflow interpretation for the filaments. Given an inclination of 20 deg, the most conspicuous part of the filaments, i.e. the central HCO$^+$ unresolved intensity peak, would lie < 80 AU above the star (from the maximum possible angular distance to the star of the blue-shifted and off-center component), at velocities < 7.2 km s^{-1} relative to the star. The bulk of the material flows at lower velocities, in fact

4

the peak is at systemic velocities (Fig. S9). Yet the line-of-sight velocity spread of HCO^+ emission from the outer disk, of 4 km s^{-1} at 1.0 arcsec, corresponds to rotation velocities of 5.9 km s^{-1} at 140 AU in the plane of the disk. The corresponding escape velocity at 80 AU is 8.6 km s^{-1}. So the bulk of this outflow cannot be ballistic (in particular the systemic-velocity filament, which extend from the star and into the outer disk). Therefore an ambient medium would be required to decelerate this hypothetical outflow. In this scheme a jet would entrain ambient molecular gas and produce the observe HCO^+ flows. However, no optical/IR jet is seen. A Brγ line is conspicuous in the stellar spectrum, but it is unresolved (see Fig. S12), so contained well within the inner 5 AU. Additionally, this molecular medium would need to be pressure-supported, as in a class I envelope, and extend vertically above the disk to $\sim$100 AU. Yet the observed SED[11] shows very little extinction ($A_V \lesssim 0.6$), consistent with interstellar values rather than intranebular extinction.

Physicality of an orthogonal inner disk   The high-velocity central flows could be thought to stem from Keplerian rotation orthogonal to the plane of the outer disk, so with an inclination of $\sim$90 deg (high inclinations are required to account for aspect ratio). However, given the outer-disk Keplerian velocities, an inner disk extending out to 0.1 arcsec but orthogonal to the plane of the outer disk should show a double-peaked spectrum with line of sight velocities $\sim$ 26 km s^{-1}, while the observed peak is at 7.2 km s^{-1}. In addition to these dynamical arguments, an orthogonal inner disk is also inconsistent with the observed CO 4.67 μm emission. This fundamental ro-vibrational transition is seen to originate from an inner disk that is aligned with the outer disk[26].

Estimates of mass inflow rates   Under the hypothesis that the observed filaments are accretion streams, we can estimate a mass inflow rate onto the inner disk. A lower limit comes from the HCO^+(4-3) observation. This line stems from gas close to the critical density, so close to $n_{H2} \sim 10^6$ cm^{-3}. The average density along the filaments is probably higher. With an inflow velocity of 5 km s^{-1}, and a filament section of $\sim$ 0.25×0.25 arcsec^2, we obtain a mass inflow rate of $dM_i/dt > 7\,10^{-9}$ M$_\odot$ yr^{-1}. The mass seen in the dust continuum provides another limit. The fraction of flux in the filaments is 1/1000, so the filaments carry $\sim 10^{-4}$M$_\odot$ for a uniform and standard dust to gas ratio. For a characteristic radial velocity < 1km s^{-1} (we do not detect the radial velocity of the filaments - only their roots are infalling), and for a liner size of 100 AU, the dynamical age of the filaments is > 474 yr. The corresponding mass infall rate is $dM_i/dt < 2\,10^{-7}$ M$_\odot$ yr^{-1}. We see that the observed stellar accretion rate[10], of 7×10^{-8} M$_\odot$ yr $^{-1}$, is bracketed within

5

one order of magnitude by the above limits on the filament mass inflow rate.

North-south asymmetry in the continuum. The most striking feature of the continuum is its horseshoe shape. Differential stellar heating, on its own, cannot account for the observed north-south contrast of 28 ± 0.5. The continuous HCO^+ ring supports that the ring has a clear view of the star, so that there is little UV opacity. In this case radiative thermal equilibrium predicts a $T \propto 1/\sqrt{r}$ radius-temperature relationship. The ratio in radius to the inner edge of the disk, as traced by the near-IR image, is at most 1.4 in the north-south direction. Since thermal submm specific intensities are in the Rayleigh-Jeans regime and so proportional to the dust temperature, for differential stellar heating we would expect a meek modulation in continuum intensities of not more than $\sqrt{1.4}$.

4 Near-IR ADI processing and search for protoplanets

HD 142527 was imaged by the Near-Infrared Coronagraphic Imager (NICI) at the Gemini South telescope in the two filters, CH4-K5%L_G0748 (2.241 μm with 107 nm bandwidth, CH4L hereafter) and CH4-K5%S_G0746 (2.080 μm with 105 nm bandwidth, CH4S hereafter), using a 0.22 arcsec semi-transparent coronagraphic mask (with 95% Lyot stop) and in pupil tracking mode (the rotator is disabled to let the field rotate and to stabilize the pupil). The total PA rotation was $\sim$40 deg. We also obtained unsaturated Brγ data, with a $\sim$20 deg rotation. Seeing and transparency conditions were good.

We reduced both CH4 channels using a set of pipelines run independently and in parallel. Each pipeline was sequentially optimized to retrieve either the disk extended emission and/or point sources.

First of all, it must be noted that face-on disks are particularly difficult to recover using ADI techniques[6], which is the case of HD 142527. Furthermore the complex disk structure makes ADI processing even more prone to artifacts. In order to obtain a confident view of the disk, we decided to perform statistical PSF averaging instead of PSF subtraction (Fig. 1 c), using the Geneva PADIP pipeline. Apart from PSF subtraction we kept all the other reduction steps, namely flat fielding, bad pixel removal, high-pass filtering, strehl based frame selection, Fourier based recentring and derotation. This way, by skipping the PSF subtraction step we get rid of most artifacts common to all ADI algorithms due to disk self-subtraction, but at the cost of a lower contrast and an increased inner working angle at

0.7 arcsec. The resulting image is a median of the best frames, corrected for field rotation.

In order to extract further details from the disk image with statistical PSF averaging we subtracted a Moffat profile fit to the stellar PSF over distinct regions in azimuth. The result is shown on Fig. S11. The final result of this conservative reduction is the most detailed view of the HD 142527 complex disk structure ever obtained (the near-IR images have finer resolution than Cycle 0 ALMA data). We caution that the arc-like structures inside 0.7 arcsec are probably artifacts. As they rotate in parallactic angle, the strongest static speckles can bias the median disk image into such arc-like features.

To optimize the search for point sources around the star within the disk gap we then ran pipelines in conventional ADI mode with sophisticated PSF subtraction algorithms. PSF subtraction had to be used in order to have access to the inner region of the disk inside 0.7 arcsec. This was achieved by running three different pipelines. The PSF reconstruction was implemented by a set of methods based respectively on the well-known ADI[7] PSF subtraction technique (PADIP), the locally optimized combination of images (LOCI[8]), and the new principal component analysis (PCA[9]). The task is particulary complex due to the disk structure in the outer regions, and to the presence of strong persistent speckles close to the star as can be seen on Fig. S12 b–f. It should be noted that artifacts caused by the ADI observing strategy do not propagate radially when reduced with all methods except for LOCI, which means that the outer disk structures will not induce artifacts in the inner cavity for all methods except LOCI.

PADIP (Fig. S12 d,g) performs parallelised frame operations in the Fourier space, with high-pass pre-filtering, subtracting optimized PSFs for each single frame, and setting priority on flux conservation. It was initially conceived to find point sources, but a new mode optimized for disk reductions, which reduces the ADI induced artifacts by using smeared PSF references, has been implemented for these observations.

The second method we used, LOCI (Fig. S12 e, h), finds the optimal linear combination of reference frames to minimize the noise in a given zone of the target image. The process is repeated until the area of interest in the target image is completely reduced. LOCI has a known tendency to generate artifacts in extended sources such as circumstellar disks. However, this defect of the generic LOCI algorithm is brought under control in a modified version. The d-LOCI algorithm[10,11] (Fig. S12 b) incorporates a fine tuning of the geometrical parameters in LOCI (such as the size of the optimization zone, the number of reference frames used in the correlation matrix, as well as the introduction of a damping

parameter through a Lagrange multiplier) to balance flux conservation with noise attenuation.

The third PSF subtraction method, based on PCA (Fig. S12 f,j)), proceeds as follows: assuming a library of reference PSFs, a Karhunen-Loève transform of these references is used to create an orthogonal basis of eigenimages, on which the science target is projected to create the reference PSF. A PSF constructed in this fashion minimizes the expected value of the least-squares distance between the ensemble of reference images and the random realization of the telescope response contained in the science image.

Small inner working angles are difficult to obtain with ADI techniques because the PA variation needed close in is too constraining. We also obtained unsaturated Brγ data sets with NICI. This data set, although taken in pupil tracking mode (PA modulation of $\simeq 20$ deg), was also accompanied by a standard star, that was used to construct a reference PSF using the PCA method for reference star differential imaging (RDI). The corresponding image is shown in Fig. S12 k.

No obvious point sources could be detected by either methods. Several hot spots are nevertheless identified, but additional follow-up to further characterize them is required. At this point it is not clear if these hot spots are related to the disk, bridges, or putative companions currently forming within the disk. Based on these reductions, we derived conservative upper limits, summarized in Fig. S13, which also give new upper limit close stellar companions within 0.1 arcsec (such as HD 142527B tentatively reported from optical interferometry, see Sec 5 below).

5 Physical considerations on close stellar companions

A non-zero closure phase from sparse-aperture-masking (SAM) near-IR data has recently[12] been interpreted in the context of binary models, which are optimal for a 0.1–0.4 M$_\odot$ companion at $\sim$13 AU (88 marcsec). Our RDI data limit such a companion to less than 0.3 M$_\odot$. The reality of this stellar companion is debatable, as the binary model for the visibility data ignores the inner disk, which accounts for the largest fraction of the near-IR flux[11]. We tested the binary model by simulating SAM observations at 2 μm on a radiative transfer prediction obtained with the MCFOST[13] package, for an azimuthally symmetric model inner disk that is consistent with the spectral energy distribution (SED). We find that even after Fourier-filtering, the visibilities from the disk in the SAM u, v coverage

reach $\sim$2 Jy (for comparison values we refer the reader to radiative transfer modeling of the observed SED[11]), while the flux density from a hypothetical HD 142527B would be down at $\sim$0.065 Jy (in K, for a magnitude difference of 4.8 and a total magnitude of 5.0). Thus deviations from axial symmetry amounting to a mere 3.25% of the total inner disk flux could account for the phase closures that have been interpreted in a binary model. The dust scattering phase function is inherently asymmetric, so that radiative transfer effects alone can reproduce the observed closure phases, even based on axysymmetric disk models. In any event, at such short separations this putative stellar companion would lead to a very different disk morphology. The cavity would be much smaller[7], and be entirely devoid of gas.

ADDITIONAL REFERENCES

1. Casassus, S. *et al.* Morphological Analysis of the Centimeter-Wave Continuum in the Dark Cloud LDN 1622. *Astrophys. J.* **639**, 951–964 (2006). `arXiv:astro-ph/0511283`.

2. Shepherd, M. C. Difmap: an Interactive Program for Synthesis Imaging. In Hunt, G. & Payne, H. (eds.) *Astronomical Data Analysis Software and Systems VI*, vol. 125 of *Astronomical Society of the Pacific Conference Series*, 77 (1997).

3. Brinch, C. & Hogerheijde, M. R. LIME - a flexible, non-LTE line excitation and radiation transfer method for millimeter and far-infrared wavelengths. *Astron. Astrophys.* **523**, A25 (2010). `1008.1492`.

4. Wootten, A., Snell, R. & Glassgold, A. E. The determination of electron abundances in interstellar clouds. *Astrophys. J.* **234**, 876–880 (1979).

5. Draine, B. T. Interstellar Dust Grains. *Ann. Rev. Astron. Astrophys.* **41**, 241–289 (2003). `arXiv:astro-ph/0304489`.

6. Milli, J. *et al.* Impact of angular differential imaging on circumstellar disk images. *ArXiv e-prints* (2012). `1207.5909`.

7. Marois, C., Lafrenière, D., Doyon, R., Macintosh, B. & Nadeau, D. Angular Differential Imaging: A Powerful High-Contrast Imaging Technique. *Astrophys. J.* **641**, 556–564 (2006). `arXiv:astro-ph/0512335`.

8. Lafreniere, D., Marois, C., Doyon, R., Nadeau, D. & Artigau, E. A New Algorithm for PointSpread Function Subtraction in HighContrast Imaging: A Demonstration with Angular Differential Imaging. *The Astrophysical Journal* **660**, 770–780 (2007). URL `http://stacks.iop.org/0004-637X/660/i=1/a=770`.

9. Soummer, R., Pueyo, L. & Larkin, J. Detection and Characterization of Exoplanets and Disks Using Projections on Karhunen-Loève Eigenimages. *Astrophys. J.* **755**, L28 (2012). `1207.4197`.

10. Pueyo, L. *et al.* Application of a Damped Locally Optimized Combination of Images Method to the Spectral Characterization of Faint Companions Using an Integral Field Spectrograph. *ApJS* **199**, 6 (2012). `1111.6102`.

11. Mawet, D. *et al.* Direct imaging of extra-solar planets in star forming regions: Lessons learned from a false positive around IM Lup. *ArXiv e-prints* (2012). `1207.6017`.

12. Biller, B. *et al.* A Likely Close-in Low-mass Stellar Companion to the Transitional Disk Star HD 142527. *Astrophys. J.* **753**, L38 (2012). `1206.2654`.

13. Pinte, C., Ménard, F., Duchêne, G. & Bastien, P. Monte Carlo radiative transfer in protoplanetary disks. *Astron. Astrophys.* **459**, 797–804 (2006). `arXiv:astro-ph/0606550`.

14. Baraffe, I., Chabrier, G., Barman, T. S., Allard, F. & Hauschildt, P. H. Evolutionary models for cool brown dwarfs and extrasolar giant planets. The case of HD 209458. *Astron. Astrophys.* **402**, 701–712 (2003). `arXiv:astro-ph/0302293`.

15. Baraffe, I., Chabrier, G., Allard, F. & Hauschildt, P. H. Evolutionary models for solar metallicity low-mass stars: mass-magnitude relationships and color-magnitude diagrams. *Astron. Astrophys.* **337**, 403–412 (1998). `arXiv:astro-ph/9805009`.
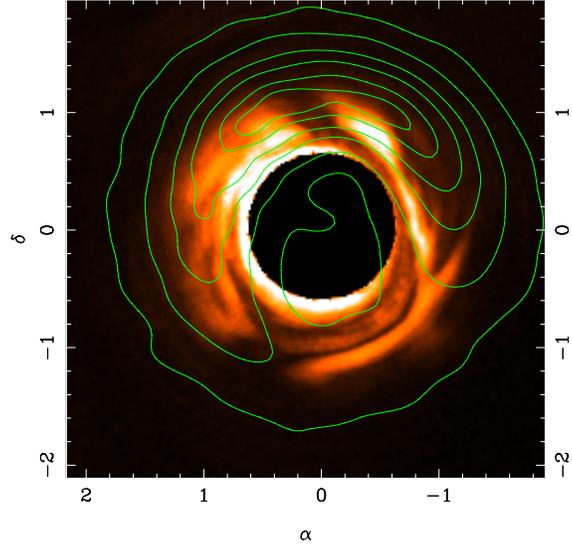
Figure S1 **Match between the radio continuum and near-IR disk**. Axis labels follow from Fig. 1. We show 345 GHz continuum, from Fig. 1a, overlaid on the 2 μm image from Fig. 1c. Contour levels for the continuum are as in Fig. 1a.
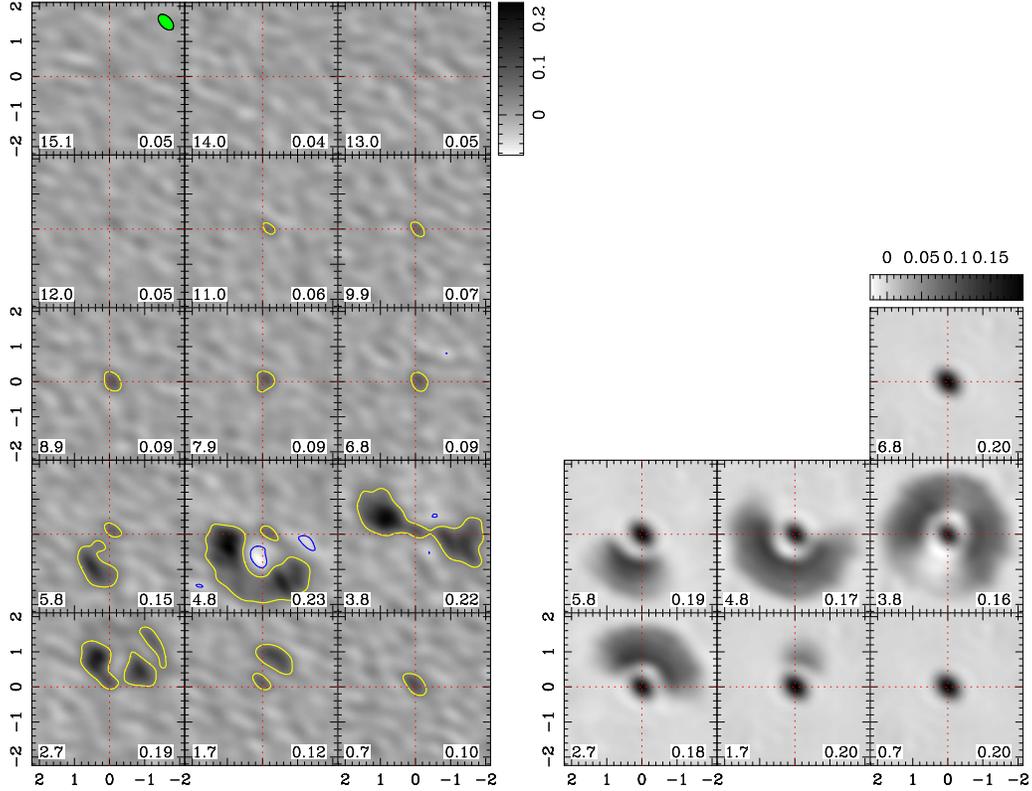
11

Figure S2 **Channel maps in HCO$^+$(4-3) highlight the high-velocity streams below 0.7 km s^{-1} and above 6.8 km s^{-1} and the gap-crossing filaments at 3.8 km s^{-1} (systemic velocity).** **a)** Left column: we show specific intensity maps from CLEAN reconstructions in exponential grey scale for velocity bins corresponding to 5-channel averages, a thin yellow contour at 4 σ and a thin blue contour at -4 σ, where 1 $\sigma = 12$ mJy beam^{-1} is the noise level. The LSR velocity is indicated at the bottom left of each image, in km s^{-1}, while the peak specific intensity is indicated at bottom right, in Jy beam^{-1}, with a beam of 0.51×0.33 arcsec^{-2} (as in Fig. 1). Axis labels for images are in arcsec; North is up, East is to the left. The cross-hairs indicate the origin. **b)** Right column: Channel maps in HCO$^+$(4-3) from the fiducial model. Same as a) but for a comparison model disk calculated with the LIME package, filtered in (u, v) coverage and reconstructed with CLEAN in the same way as for the ALMA observations. We have added a central Gaussian to the LIME model, which is intended to illustrate that beam elongation effects cannot join this central component with the outer disk. *Continues in Fig. S3*
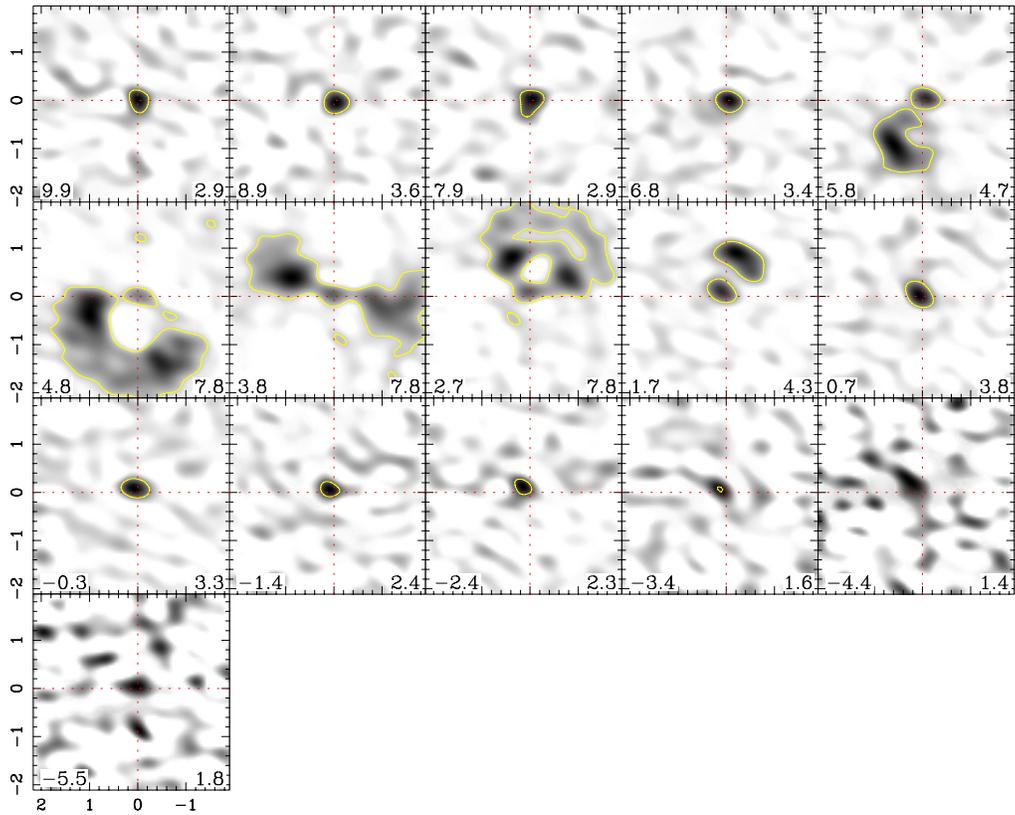
12
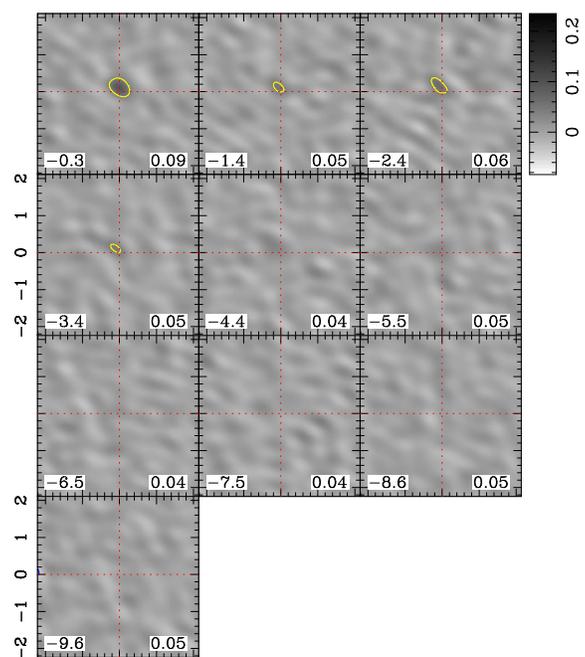
Figure S3 *continues from Fig. S2*

Figure S4   Channel maps in HCO$^+$(4-3) from deconvolved models. Same as Fig. S2 but for a deconvolved MEM model of the data rather than the restored CLEAN images. Peak intensity values are indicated in 10^4MJy sr^{-1}. Notice the gap-crossing filaments seen in systemic velocity, at 3.8 km s^{-1}. We use a reference 1 σ value of 3090 MJy sr^{-1}. To convert into specific intensity units used for the restored imaged (convolved with the CLEAN beam), these MJy sr^{-1} must be multiplied by $4.48\ 10^{-6}$.

14
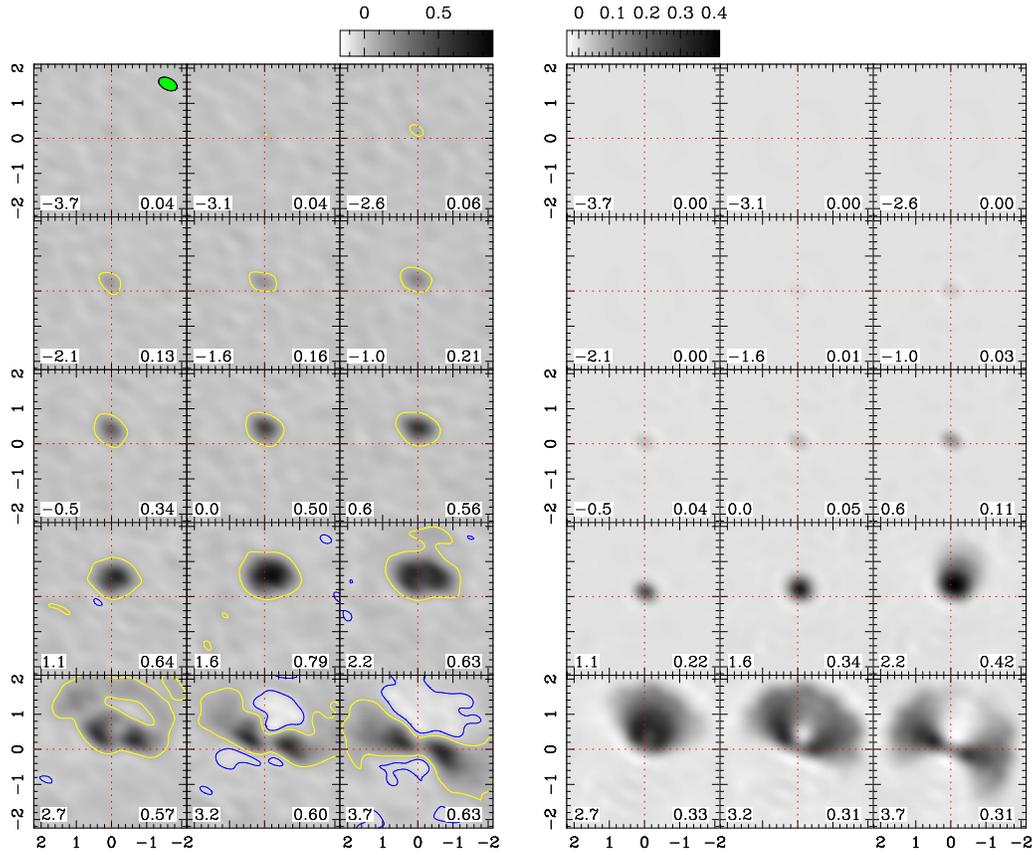
Figure S5   Channel maps in CO(3-2). Labels follow from Fig. S2. **a)** Left column: we show specific intensity maps in grey scale for 28 velocity bins corresponding to 5-channel averages, with a yellow contour at 5 σ and a blue contour at -5 σ, where 1 σ=0.011 Jy beam^{-1}. The LSR velocity is indicated at the bottom left of each image, in km s^{-1}, while the peak specific intensity is indicated at bottom right, in Jy beam^{-1}, with a beam of 0.51×0.33 arcsec^{-2} (as in Fig. 1). Axis labels for images are in arcsec; North is up, East is to the left. The cross-hairs indicate the origin. **b)** Right column: same as Fig. S5 but for a comparison model disk calculated with the LIME package, filtered in (u, v) coverage and reconstructed with CLEAN in the same way as for the ALMA observations in a). *Continues in Fig. S6*
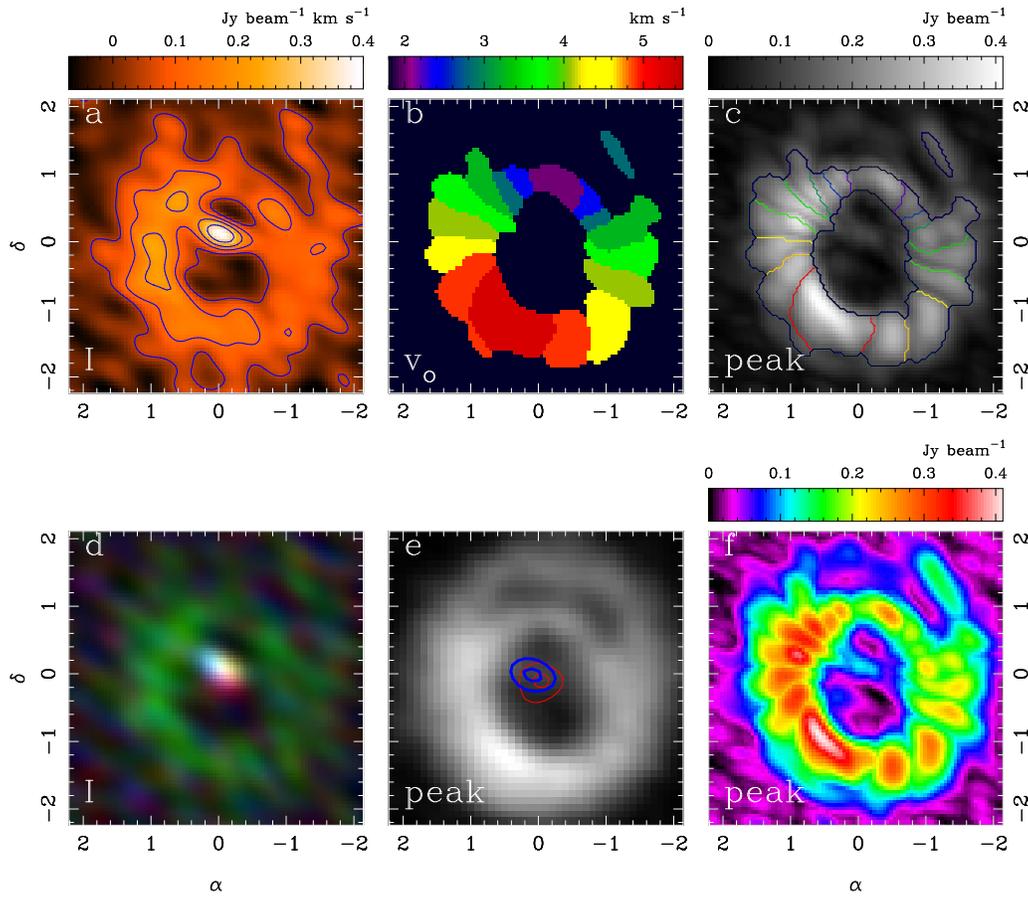
15
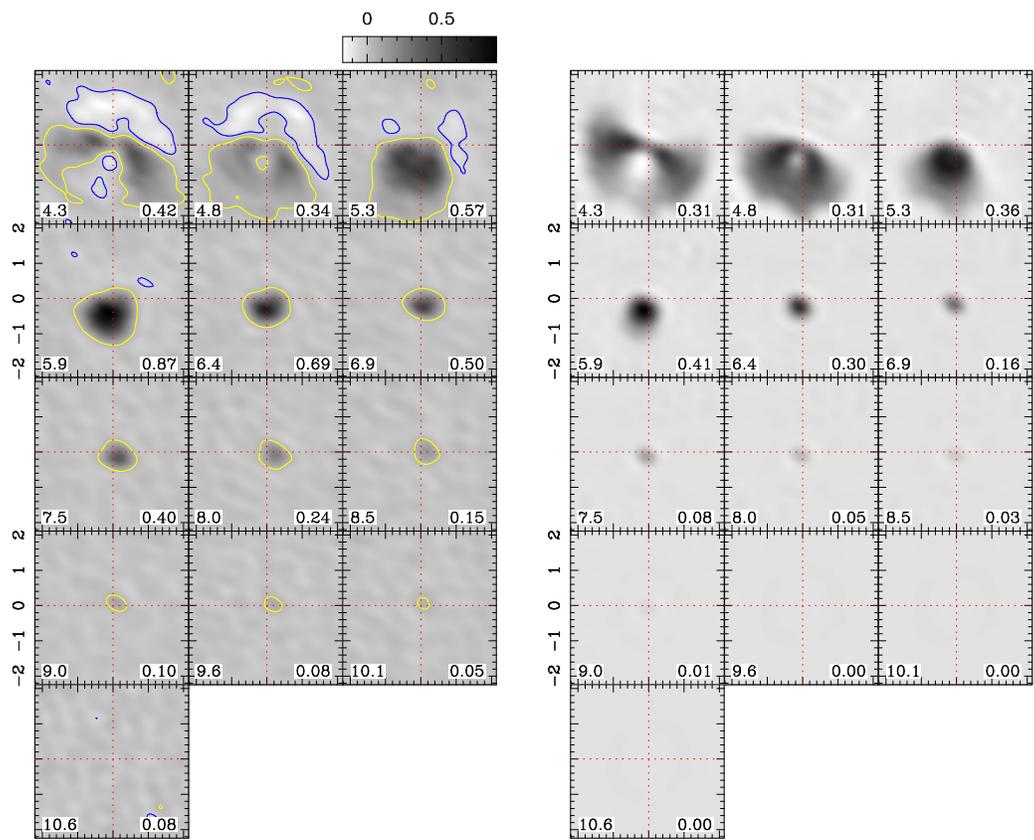
Figure S6 *continues from Fig. S5*

Figure S7 **HCO$^+$(4-3) maps**. Axis labels for images are in arcsec; North is up, East is to the left. The origin of coordinates is centred on the star. The beam size is 0.51×0.33 arcsec^{-2} (as in Fig. 1) **a:** Intensity map, highlighting that the peak is found near the center. Contour levels are as in Fig. 1c. **b:** LSR velocity of the peak emission. **c:** Peak intensity map, showing a whole ring. The modulation along the ring that leads to a segmented appearance is due to the 5-channel average, as indicated by the exact overlap with the channel boundaries. Countours indicate LSR velocity, with colour codes that match b). **d:** RGB intensity image, with the Keplerian velocities ($1 \leq v/$km s$^{-1} \leq 5.9$) in green, and the high velocity flows in red ($11.5 > v/$km s$^{-1} > 5.9$) and blue ($1 > v/$km s$^{-1} > -4$). **e:** Peak intensity taken on a CLEAN reconstruction of the original data, without channel averaging, and with subsequent smoothing by 0.2 arcsec. As a consequence of the fine sampling, the central filamentary flows are not as obvious as in the 5-channel

17

average, but the outer ring is less segmented. Contours correspond to blue (-4.5 to +1.3 km s^{-1}) and red (+5.6 to +10 km s^{-1}) intensity, and are taken at fractions of 0.5 and 0.9 of each peak. **f:** peak intensity, as in c), but highlighting the central eastern bridge in false colour and exponential scale. The segmented appearance is due to the 5-channel average.
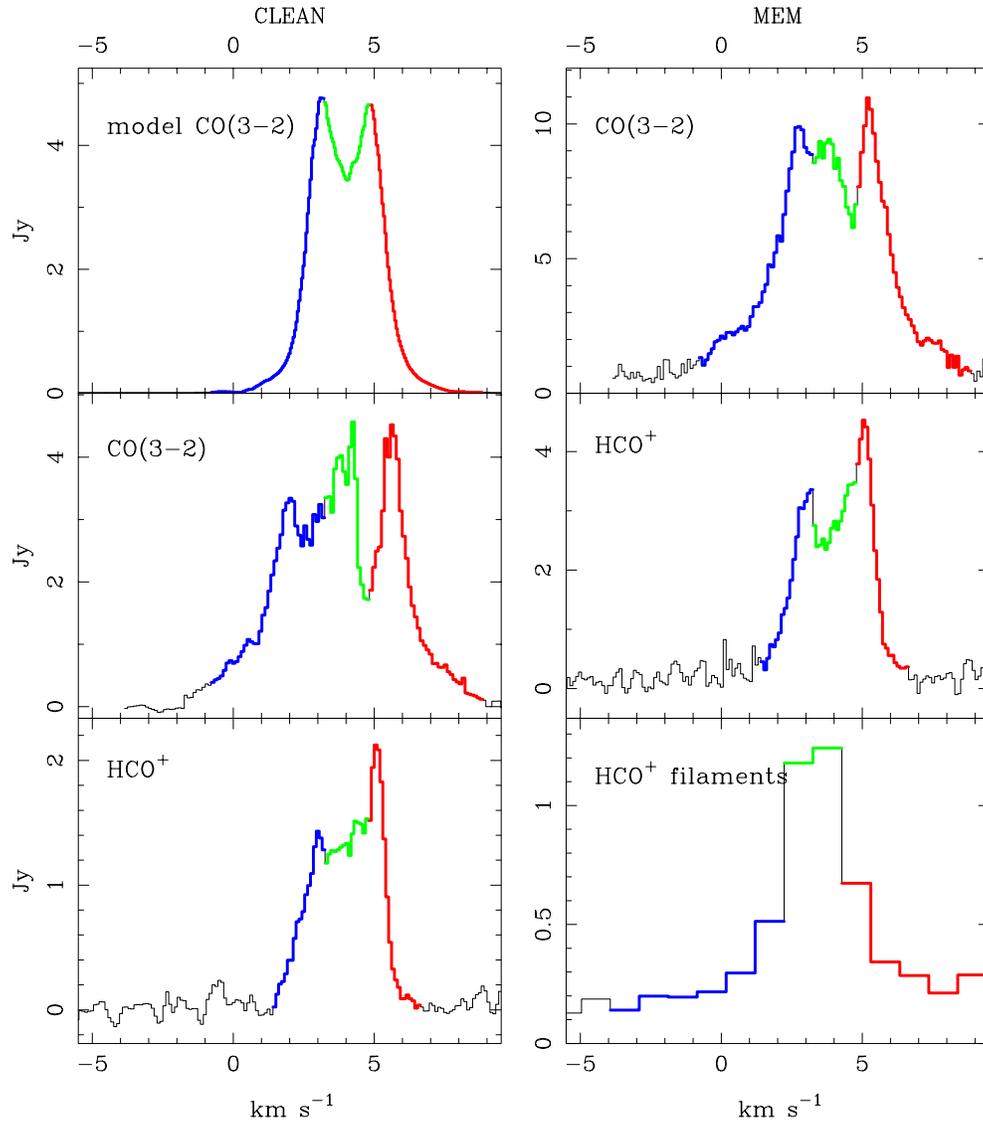
Figure S8 **Spectra extracted from the RGB images shown in Fig. 1**. These spectra are meant to inform the definition of the RGB velocity codes, and are extracted over apertures defined by the field of view of the comparison RGB images. These spectra do not represent accurate measures of the total integrated spectrum. Comparison with previous work[9] at coarser resolutions shows that these extractions are modulated by flux loss and CLEAN artifacts. Left column shows CLEAN reconstructions, while right column shows MEM reconstructions. Labels indicate flux density in $y-$axis, in Jy, and v_{LSR} in $x-$axis, in km s^{-1}. Notice the irregular blue peak in CO(3-2), which is modulated by CLEAN artefacts (extended negatives to the north). Our MEM recovers more flux but is noisier in individual channels of this dataset. Note also that the comparison model CO(3-2) spectrum is sensitive on the adopted temperature profile, so is shown here only as a reference Keplerian rotation model. The spectrum labels correspond to the following figures: 'model CO(3-2)', Fig. S10; 'CO(3-2)', Fig. 1 b; 'HCO$^+$', Fig. 1 d; 'filaments', inset to Fig. 1 d.
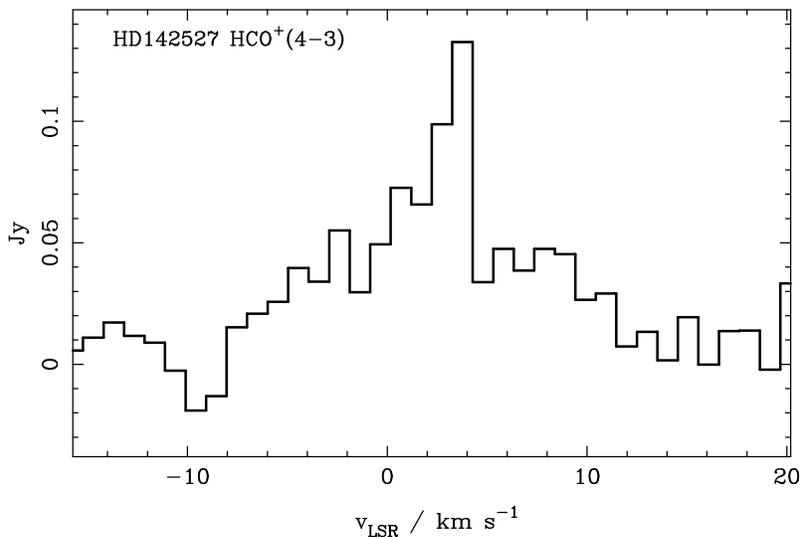

Figure S9 **HCO$^+$ spectrum extracted from the central intensity peak**. The aperture size is 0.5×0.6 arcsec.
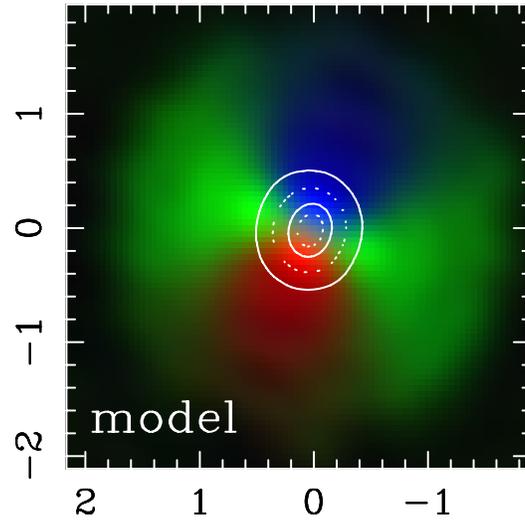
Figure S10 **Prediction for CO(3-2) from a fiducial disk model for comparison with the velocity field coded in RGB in Fig. 1**. This prediction has been filtered by the ALMA uv-coverage and reconstructed with CLEAN, in the same way as the observations. Axis labels and color codes follow from Fig. 1b.
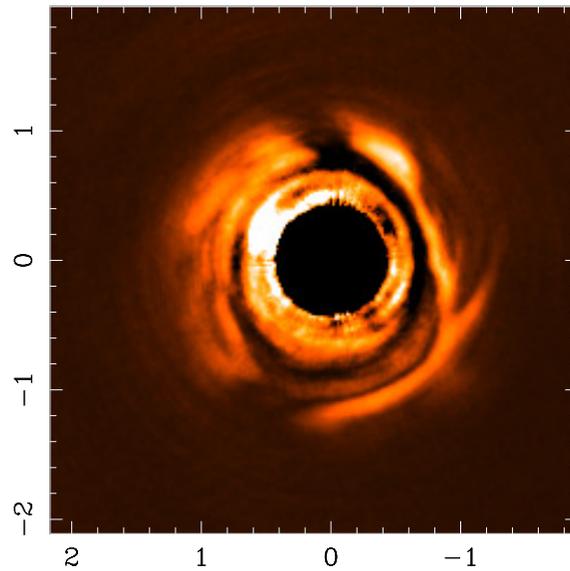
Figure S11 **Gemini NICI image of the disk with approximate PSF-subtraction**.
This image shows the CH4S filter, with PSF averaging and derotation. It shows
the least biased disk image, as Fig. 1 c, but with approximate PSF subtraction
using an azimuthally-varying Moffat profile fit to the PSF halo. The spiral structure
seen inside the cavity (immediately surrounding the intensity mask) is probably
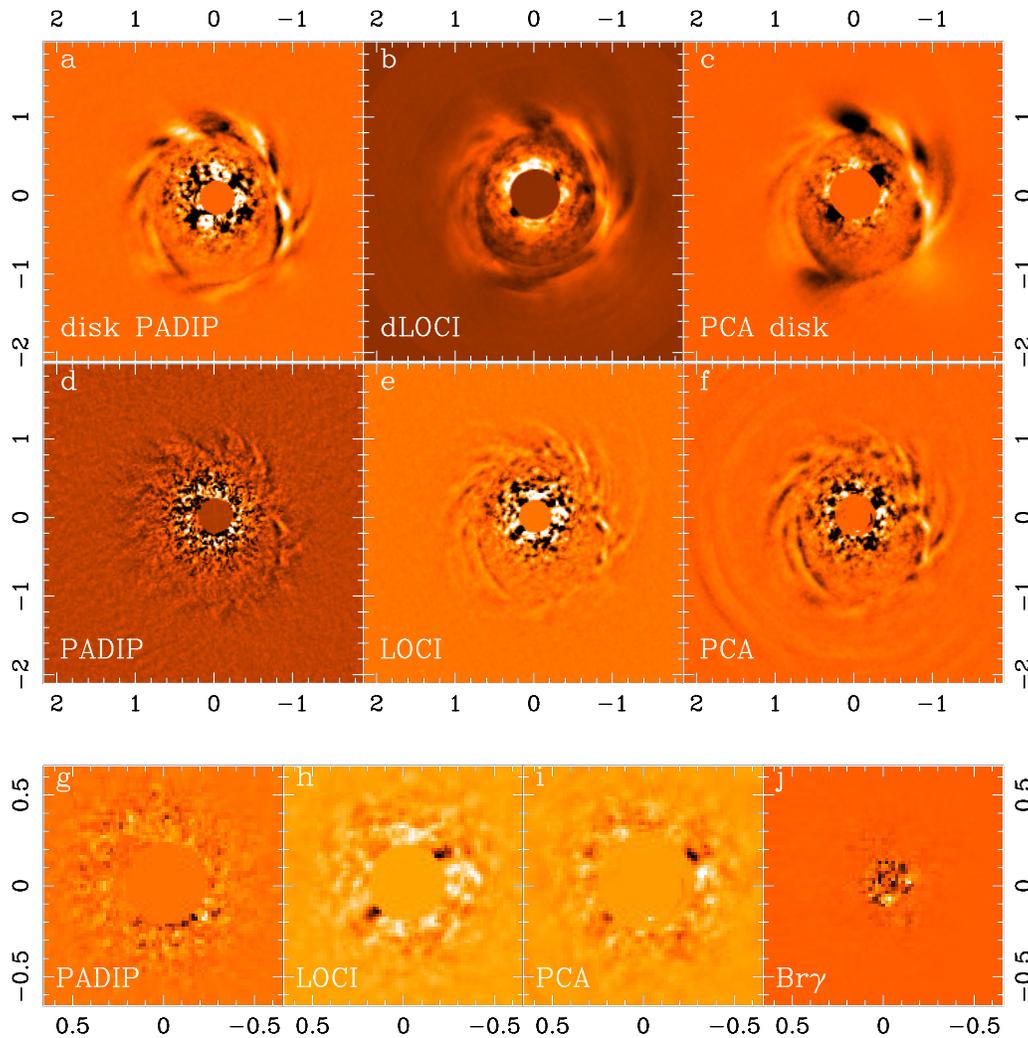the result of strong static speckles in these ADI data.

Figure S12 **Gemini NICI images after various PSF-subtraction methods**. All pan-
els show the CH4S filter (an analogous set of images is available in CH4L), except

for j). **a:** PADIP pipeline image of the disk. **b:** Damped-LOCI image of the disk. **c:** PCA image of the disk.**d:** Aggressive PADIP image for faint companion search. **e:** Aggressive LOCI image. **f:** Aggressive PCA image. **g:** Aggressive PADIP zoom. **h:** Aggressive LOCI zoom. **i:** Aggressive PCA zoom. **j:** Brγ RDI limits close-in stellar companions - this last image was reduced with PCA, its IWA is only 50 mas, as opposed to 220 mas in CH4S.
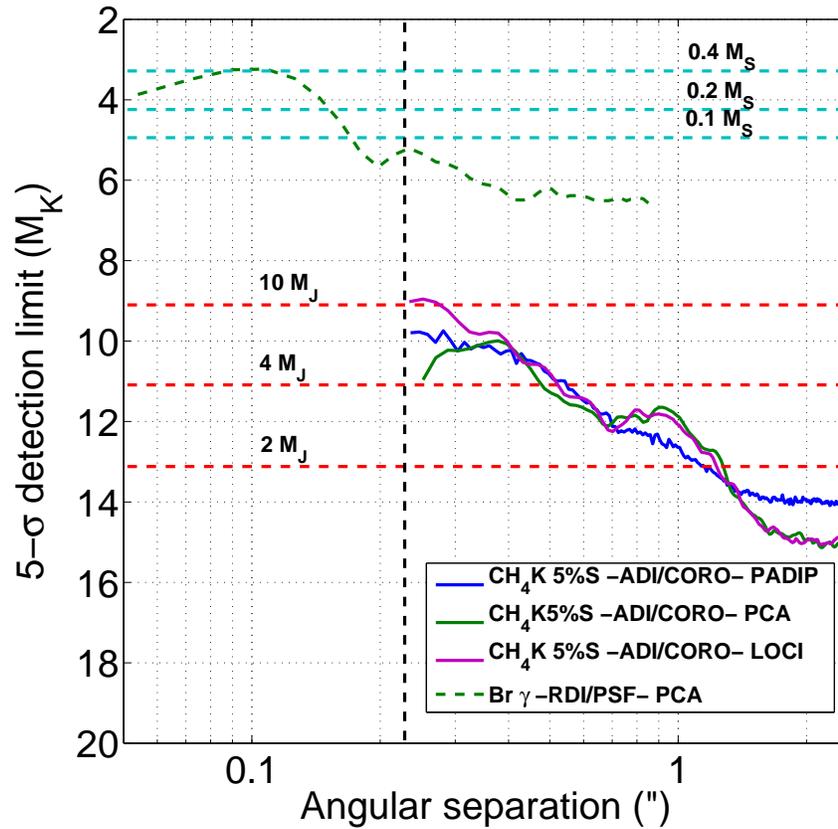

Figure S13 **Limits on companion mass from NICI CH$_4$ ADI, and NICI $Br\gamma$ reference star differential imaging (RDI)).** For NICI CH$_4$ ADI, we report contrast curves in three different techniques (PADIP, LOCI and PCA, see text for details). These limits are not corrected for extinction. As a comparison point we refer to the COND03[14] tracks at 2 Myr of age, which lead to the mass upper limits indicate on

the plots. The vertical dashed black line indicates the effective inner working angle, set here by the extent (0.22 arcsec) of the semi-transparent Lyot coronagraph used in the NICI CH$_4$ ADI data set. The NICI $Br\gamma$ detection limits obtained with RDI are also indicated along with 2 Myr stellar tracks using the BCAH98 model[15].